NDT&E International 131 (2022) 102682

Contents lists available at ScienceDirect

NDT and E International

journal homepage: www.elsevier.com/locate/ndteint

Rapid non-destructive sizing of microstructural surface integrity features using x-ray diffraction

Matthew Brown *, Pete Crawforth, David Curtis

University of Sheffield Advanced Manufacturing Research Centre, Advanced Manufacturing Park, Wallis Way, Catcliffe, Rotherham, S60 5TZ, UK

A B S T R A C T

In this study, rapid non-destructive sizing of machining-induced subsurface white layers and plastic deformation is achieved through x-ray diffraction peak breadth measurements. Sizing to within 0.5–2 μm is shown to be possible for features thinner than the x-ray penetration depth with inspection times under 1 min achievable. Whilst the technique can detect features larger than the penetration depth, accurate sizing is not possible. Appropriate selection of different x-ray radiation and diffraction peaks can be used to increase or decrease the penetration depth to improve sizing accuracy at larger and thinner feature thicknesses, respectively. However, there is a depth limit for each material imposed by the smallest wavelength of radiation that can be used and the highest angle diffraction peak that can be resolved. The dependence of peak breadth on deformation or white layer thickness can be modelled by assuming a linear or exponential decay in strain across the feature thickness.

1. Introduction

Machining of difficult-to-machine aeroengine alloys such as titanium, nickel superalloys and hardened steel can result in the formation of anomalous surface integrity features such as white layers and swept grains in the near-surface. The assessment of these features is a vital step in the validation of a manufacturing process, as research has shown that their presence in an aeroengine component can have a significant effect on functional performance and expected life in service [1,2].

Machining-induced white layers are generated via one of two mechanisms [3], phase transformation (PT) or severe plastic deformation (SPD) which can involve dynamic recrystallization. These layers are typically characterised as a region of low ductility material [4] which possesses an ultra-fine grain size [5], high hardness [6] and extremes of residual stress [7]. In industry, the white layer is often defined as a region in the machined subsurface in which the microstructure cannot be distinguished from the bulk microstructure. It has been reported [2] that the presence of a 10 μm white layer can reduce the fatigue life of a drilled component by as much as 10 times compared to the benchmark life, even after shot-peening. As such, the presence of any white layer in an aeroengine component, regardless of thickness, is typically considered unacceptable. PT white layers are formed when thermal effects dominate the cutting operation, for example when machining with very high cutting speeds and dry cutting [8]. For SPD white layers, formation is dictated by deformation rather than temperature effects and, as such, they are associated with high tool wear [9].

Swept grain (also called distorted layer or surface drag) is the plastic deformation of the material in the near-surface of a workpiece in the direction of the cutting velocity, without recrystallization [10]. As such, swept grain appears as the distortion of the grain structure in a cross-sectional micrograph, but due to the lack of recrystallization, the grain size is unaffected. Similar to SPD white layers, swept grain formation is typically associated with worn tooling [11] and can be enhanced at both higher [12] and lower [13] cutting speeds, depending on the material being deformed and the deformation modes involved. The thickness of the swept grain region is defined by the average or maximum depth to which grain distortion can be observed, however, due to the subjectivity in determining the extent of the deformed region, there is a degree of uncertainty in the depth measurement. This has been demonstrated experimentally in recent work by Sela et al. [14] where it was shown that the depth of deformation measured using micro-grids etched into the workpiece was larger than that quantified using cross-sectional microscopy.

Due to plastic deformation in the primary and tertiary shear zones during chip formation, the workpiece is always deformed when machining. As such, the presence of swept grain should be expected in all machined surfaces, although in some materials the depth of the deformed layer may be too small to resolve. Swept grain thickness can vary from layers thinner than 3 μm in gentle machining [10] up to layers over 250 μm thick under extreme deformation during abusive machining [15]. In contrast to white layer inspection, swept grain inspection is typically dependent on both the thickness of the layer and the

* Corresponding author.
E-mail address: m.o.brown@amrc.co.uk (M. Brown).

https://doi.org/10.1016/j.ndteint.2022.102682
Received 1 April 2022; Accepted 31 May 2022
Available online 7 June 2022

alloy under investigation, this is because Herbert et al. [2] have shown that, depending on the alloy, low levels of swept grain, e.g. 10 μm or less, have a negligible influence on the fatigue performance, whereas for thicker swept grain layers, a measurable decrease in fatigue life can be recorded. In white layers formed by SPD, a swept grain region would always be expected beneath, due to the gradual decay of imparted strain with depth beneath the surface, which does not drop to bulk levels outside of an SPD white layer [16]. By contrast, in PT white layers, where temperature effects dominate, a dark layer, containing tempered material which has reached a temperature sufficient for tempering but below the phase transformation temperature, is present beneath the white layer.

Previous research into the non-destructive detection of metallurgical surface integrity features has identified that x-ray diffraction (XRD) peak broadening can be used to detect the presence of white layers in milled and turned surfaces [17] as well as swept grain formed during grinding [18]. The sensitivity of XRD to white layers has been attributed to the ultrafine grain size and high levels of plastic strain which are well-known characteristics of this feature [19]. Whilst Naskar and Paul [18] did not discuss the relative contributions of size and strain broadening effects for detection of swept grain, it can be inferred from the micrographs presented that the broadening effect was due solely to strain broadening effects as the grain size in the plastically deformed layer was larger than 200 nm, an approximate crystallite size below which size broadening becomes significant [20].

Brown et al. [17] showed that the breadth of an XRD peak, its full-width at half maximum (FWHM) intensity, is larger in a surface with a white layer, such that anomalous surfaces could be distinguished from undamaged as-machined material in three different aeroengine alloys. Naskar and Paul [18] then showed that x-ray diffraction FWHM is also sensitive to plastic deformation and were able to use a grazing incidence XRD (GI-XRD) methodology to size the thickness of the deformed layer to an average deviation of 1.2 μm (root mean square error (RMSE) calculated to be 1.7 μm), for samples with deformation thicknesses between 4 and 12 μm. In the GI-XRD study, multiple different angles of incidence between 1 and 30° were used to obtain peak breadth measurements at different penetration depths, as the x-ray penetration depth is a function of the angle of incidence of x-rays on a surface [20].

The work by Naskar and Paul [18] has shown that non-destructive detection and quantification of grinding-induced deformation is possible, however, the equipment utilised was a lab-based PANalytical Empyrean diffractometer. This equipment is not practical for machined component validation in industry, due to the sample size limitations imposed by the beam optics and the radiation shielding enclosure [21]. The reliance on GI-XRD in the grinding deformation sizing method means that inspection of non-flat samples will pose significant challenges. This is because in GI-XRD the angle of incidence of the x-rays is low and therefore the illumination area and height deviation of the x-rays on curved surfaces is larger for the same incident beam optics, leading to increased instrument broadening. To counteract this, the x-ray beam can be restricted using slits, however, this reduces the intensity of x-rays reaching the surface, significantly increasing the measurement time compared to higher angle measurements in Bragg-Brentano ($\theta - 2\theta$) geometry. Naskar and Paul [18] do not give details on the measurement acquisition time for the GI-XRD measurements or indicate whether different diffraction slits were used to attempt to correct for the instrument broadening which occurs at low angles of incidence.

This study aims to expand on the previous work undertaken by Brown et al. [17] and Naskar and Paul [18] to demonstrate truly non-destructive detection of machining induced white layers and swept grain using rapid θ-2θ geometry measurements. In addition, this work will outline research undertaken to enable the quantification of feature sizes using single-exposure measurements for fast sizing, as well as alternatives to GI-XRD for changing the depth of penetration to allow sizing when feature thickness exceeds the x-ray penetration depth. Machining trials will be used to generate three different sample sets for non-destructive testing, containing SPD and PT white layers, and swept grain surfaces. The work will focus on nickel-based and steel aeroengine alloys as both previous studies [17,18] have been centred on titanium and there are differences in crystal structure and x-ray tube compatibility between the alloys.

2. Methodology

In conventional θ-2θ XRD geometry, the angle of incidence (α) and exit angle (ω) are equal and are constant ($\alpha = \omega = \theta$) for a particular material, peak and x-ray radiation combination. The x-ray penetration depth, described by Eq. (1), is therefore constant in this geometry. In Eq. (1), δ is the penetration depth, μ is the linear attenuation coefficient, $I(L)$ is the intensity at a depth L below the surface, I_0 is the intensity of x-rays at the surface. The ratio $I(L)/I_0$ defines the intensity fraction at the penetration depth, e.g. 0.05 for 95% attenuation.

$$\delta = -\frac{\ln\left(\frac{I(L)}{I_0}\right)}{\mu\left(\frac{1}{sin(\alpha)} + \frac{1}{\sin(\omega)}\right)} \tag{1}$$

Whilst it may be possible to infer the size of features from a diffraction pattern obtained at a particular depth when the feature is thinner than the x-ray penetration depth, due to relative contributions from the feature and the bulk, detection of features larger than the penetration depth poses additional challenges, as the x-ray beam is diffracted entirely within the feature. Therefore, to enable the sizing of larger features, the penetration depth can be expanded to compare the peak breadths at different penetration depths. It should be noted that GI-XRD, as shown by Naskar and Paul [18], cannot increase the penetration beyond the maximum depth achieved in θ-2θ geometry. Therefore, alternative methods must be employed in such cases where larger depths of inspection are required.

It can be seen from Eq. (1) that penetration depth is affected by both the angle of incidence and the linear attenuation coefficient. In θ-2θ geometry, where $\alpha = \omega$, the diffraction angle can be altered by inspecting a different diffraction peak as this angle is directly related to the interatomic spacing of the crystallographic plane under inspection [22]. The linear attenuation coefficient is a function of the wavelength of the x-ray radiation [20], therefore the x-ray radiation can be changed to facilitate inspection at a different penetration depth. As such, it is apparent that the penetration depth of the x-rays into a material can only be changed by changing the diffraction angle or the x-ray radiation, as the material under inspection has fixed composition and density, and these are the approaches trialled in this study.

The resultant peak breadth for a surface can be modelled as a function of the peak breadths of the material within the feature and the material outside of the feature, within the x-ray penetration depth, weighted by the fraction of x-rays diffracted within each region. X-rays decay exponentially with the distance travelled through a material, as described by Eq. (2).

$$I(x) = I_0 e^{-\mu x} \tag{2}$$

Using this knowledge of the decay of x-rays with depth, an equation describing the resultant peak breadth can be stated, as in Eq. (3), where $FWHM_L$ is the resultant peak breadth up to a depth L and $FWHM(x)$ is the peak breadth at a distance x beneath the surface. This physical meaning behind this equation is illustrated in Fig. 1 and can be understood as the average peak breadth over a small depth range multiplied by the exponential intensity weighting factor for the same depth range summed up for all depth ranges over the full depth of penetration of the x-rays L. This is then normalised by dividing by the total area under the weighting curve. The resultant equation describing the dependence of peak breadth on the feature thickness can then be evaluated by defining a relationship describing the peak breadth profile for a surface integrity

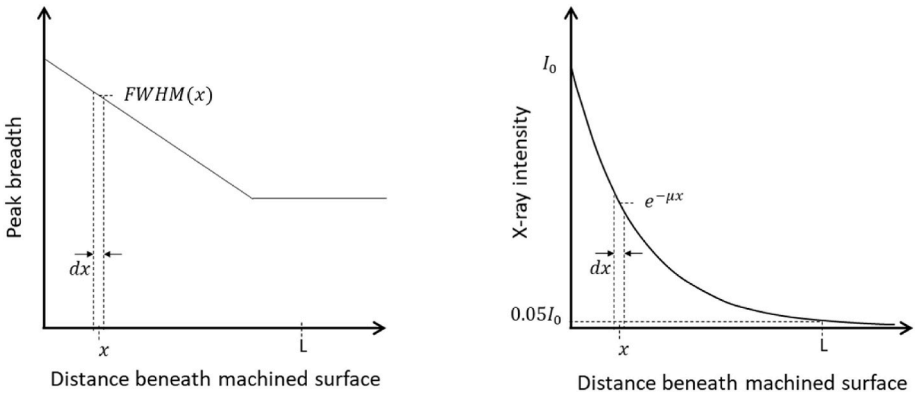

Fig. 1. Plots showing the dependence of peak breadth on depth beneath the surface (assuming linear decay with depth until the bulk peak breadth is reached) and the exponential decay of x-rays with depth.

feature, $FWHM(x)$.

$$FWHM_L = \frac{\int_0^L FWHM(x)e^{-\mu x}dx}{\int_0^L e^{-\mu x}dx} \tag{3}$$

As already highlighted, studies [16,23] have shown that the plastic strain in the machined surface can decay either exponentially or linearly with depth. As such corresponding models can be proposed for linear (Eq. (4)) or exponential strain decay (Eq. (5)), where t is the layer thickness and c is the fraction of surface strain below which there are no significant changes to broadening, e.g. a value of 0.05 was used throughout this study. The strain profile through the white layer has not been measured experimentally to date, however, nanoindentation measurements [19] show that the hardness can decay with depth through the white layer or remain largely constant across the thickness, which suggests that in certain cases, work hardening may be constant across the white layer. Additionally, peak broadening in the white layer also arises due to a small grain size, which may remain largely constant across the width of the features. Therefore, the inclusion of a model in which induced peak broadening could be constant through the feature before dropping to a lower value in the bulk material (Eq. (6)) is appropriate for consideration. In this study, these models are fitted to the experimental peak breadth data and the RMSE between the thickness predicted by the model and the measured result from microscopy is quantified. A select number of models were then validated by training a feature sizing curve with 60% of the experimental data and estimating the feature size for the remaining 40% with an RMSE between the predicted and microscopy feature thicknesses calculated. This training and validation split was repeated ten times to give an overall accuracy for the method.

$$FWHM_{Linear}(x) = FWHM_{surf} + \frac{\left(FWHM_{bulk} - FWHM_{surf}\right)}{t}x \tag{4}$$

$$FWHM_{Exponential}(x) = FWHM_{bulk} + e^{-\left(\frac{\ln(c)}{t}\right)x}\left(FWHM_{surf} - FWHM_{bulk}\right) \tag{5}$$

$$x < t,\ FWHM_{constant}(x) = FWHM_{surf}\ x > t,\ FWHM_{constant}(x) = FWHM_{bulk} \tag{6}$$

SPD white layers for XRD inspection were generated in Super CMV steel by turning the outside diameter of a 150 mm diameter tube on a Cincinnati Hawk 300 lathe using a PDJNL2020K15JETL tool holder in combination with DNMG 150608 coated carbide inserts with various levels of artificial wear, both provided by Seco tools AB. Cutting speeds were varied between 60 and 180 m/min with the depth of cut and feed rate held constant at 0.5 mm and 0.15 mm/rev. Hocut 795B (concentration 6–8%) was used as the cutting fluid and was supplied through-tool at a pressure of 80 bar. Full details of the artificially worn inserts are described in a previous paper [24]. Worn inserts were used to maximise deformation effects over thermal effects [25].

PT white layer generation was undertaken on AISI52100 steel using a DMG Mori NLX2050 with a Sandvik PTGNL 2020K 16HP tool holder and PCBN-TNGA160408S01030A 7015 triangular inserts. Unworn tooling, high cutting speeds (110–800 m/min) and dry cutting were used to promote significant heat generation in the near-surface, as PT white layers have been shown to form under these conditions [26]. Trials were performed using depths of cut of 0.08–0.25 mm and feeds of 0.075–0.125 mm/rev.

Samples containing different levels of plastic deformation were created by face turning RR1000 using a Hermle C52 five-axis vertical CNC machining centre with cutting speeds in the range 50–300 m/min, depth of cut between 0.15 and 0.5 mm and feed rates of 0.1–0.3 mm/rev. For these trials, both carbide and CBN inserts were used to allow cutting across the full range of desired speeds with new and worn tooling used to deliberately generate surfaces with low and high levels of plastic deformation, respectively. Tooling from five different suppliers were used to maximise the potential variation in surface integrity. Hocut 795B at a concentration of 6–8% was used as the metalworking fluid and was supplied through the tool at a pressure of 20 bar. A summary of the sample sets generated and the investigations they were used for is given in Table 1.

To investigate the truly non-destructive detection of thin machining induced surface integrity features, where feature thickness is smaller than the penetration depth, a Proto iXRD portable residual stress diffractometer (shortened to iXRD in this study), as shown in Fig. 2, was used to capture diffraction patterns in the vicinity of a single diffraction peak in the different sample sets. The instrument set-up for each material group is summarised in Table 2. The x-ray radiation for each alloy under inspection was selected to avoid fluorescence effects and to maximise the diffraction angle at which the peak was observed. Peak broadening is greater at higher diffraction angles, maximising the resolution of the peak breadth measurement compared to the angular resolution of the diffractometer. The diffraction patterns were fitted with a Pseudo-Voigt distribution and the FWHM peak breadth extracted. For each surface, three measurements were undertaken to quantify the uncertainty in the XRD measurements.

Table 1
The sample sets used to investigate sizing.

Sample set	Material	Features	Depth range	Investigation
A	Super CMV	SPD white layer	0–12 μm	Sizing of white layers
B	EN31	PT white layer	0–5 μm	Sizing of white layers
C	RR1000	Plastic deformation	5–60 μm	Sizing of plastic deformation

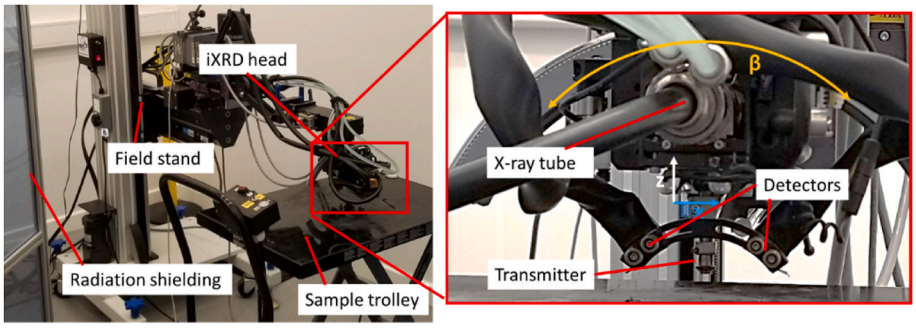

Fig. 2. The Proto iXRD as for the measurements. The x, y and β axis of head movement are illustrated.

Table 2
A summary of the Proto iXRD instrument set-up during the non-destructive surface integrity assessment of machined samples.

Sample set	X-ray radiation	Diffraction peak	Diffraction Angle (°)	Exposure time (s)	No. of exposures	Aperture (mm)
A, B	Cr- Kα	BCC – (211)	153	2	5	1 x 5
C	Mn-Kα	FCC – (311)	154	2	5	1 x 5

A PANalytical X'Pert^3 Powder (shortened to X'Pert^3 in this study) fitted with a Cu x-ray tube was used to investigate sizing using different x-ray radiation and diffraction angles as Cu x-rays have reduced penetration compared to Cr and Mn x-rays. Measurements using Cu x-rays were only possible due to the monochromator on the X'Pert^3 which reduces the impact of fluorescence of nickel and steel samples under Cu x-rays, something not possible with the iXRD which does not have similar beam optics. A PANalytical Empyrean multi-purpose diffractometer (shortened to Empyrean in this study) fitted with an Ag x-ray tube was also used for sizing as Ag x-rays have a much shorter wavelength than other typical x-ray tubes, thereby allowing for inspection to even greater depths. The inspection parameters for the X'Pert^3 and Empyrean measurements are defined in Table 3. The relative penetration depths (95% attenuation) for different x-ray radiation, diffraction peaks and angles of incidence are shown in Fig. 3 for a nickel superalloy.

Both PANalytical diffractometers are designed for lab-based measurement on powders and are not optimised to the inspection of real engineering components. They were used in this study to illustrate the potential for sizing. Cu and Ag x-rays are available for portable diffractometers such as the Proto iXRD and the larger Proto LXRD respectively, facilitating truly non-destructive measurements at different penetration depths. Note that the exposure times are much longer for the X'Pert^3 and the Empyrean compared to the iXRD due to beam optics which ensure a higher quality but lower intensity beam, the need to suppress fluorescence and the smaller detector ranges which mean the goniometer needs to be stepped to capture the full peak, rather than capturing in a single exposure.

To validate the results of NDT inspection, microscopy was undertaken on cross-sectional samples of the machined surfaces. It should be noted that optical microscopy is only capable of capturing deformation across a single plane perpendicular to the machined surface in the region of the sectioning cut. By contrast, XRD interacts with a volume of near-surface material and therefore represents the average deformation of the region illuminated by x-rays. As such, it was important to assess the surface integrity using several micrographs to better quantify the variation in surface integrity across the x-ray interaction volume.

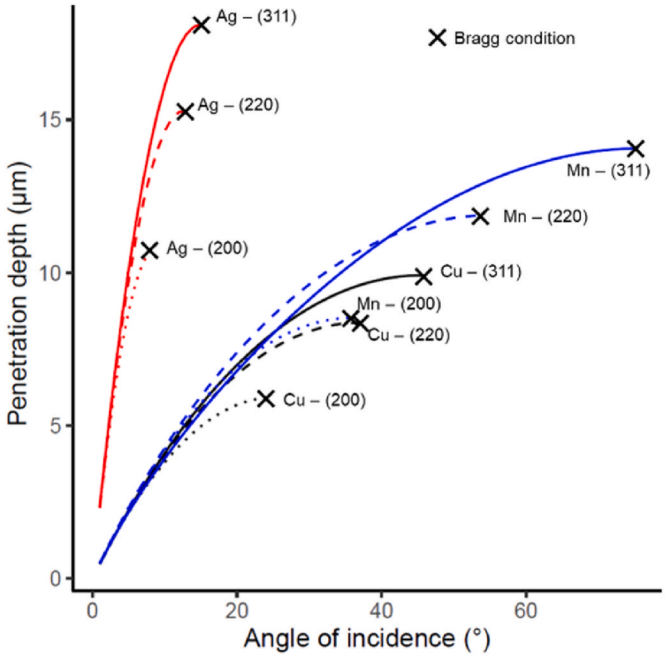

Fig. 3. X-ray diffraction penetration depths for different radiation, diffraction peaks and angles of incidence.

Table 3
A summary of the X'Pert^3 and Empyrean instrument set-up during the investigation into sizing by changing the penetration depth. (Samples set A – EN31 and Super CMV, samples set B -RR1000).

Sample set	Diffractometer	X-ray radiation	Diffraction peak	Diffraction Angle (°)	Exposure time (s)	Slits (°)
A, B	X'Pert^3	Cu- Kα	BCC – (211)	82	400	½, 1
A, B	Empyrean	Ag- Kα	BCC – (211)	28	60	¼, ½
C	X'Pert^3	Cu-Kα	FCC – (200)	51	200	½, 1
C	X'Pert^3	Cu-Kα	FCC – (220)	74	300	½, 1
C	X'Pert^3	Cu-Kα	FCC – (311)	91	200	½, 1
C	Empyrean	Ag-Kα	FCC – (311)	30	80	½, 1

3. Results

To investigate white layer detection and sizing, Super CMV and EN31 samples sets, containing SPD and PT white layers respectively, were inspected using the proto iXRD with Cr x-rays, for truly non-destructive measurement of peak breadth. The measured peak breadth has been plotted against the white layer thickness measured from cross-sectional microscopy in Fig. 4 and the three peak breadth models (Eq. (4) - Eq. (6)) have been fitted to the data. These models could be used as sizing curves for predicting feature thickness.

Of the three models fitted to the data, the exponential model gives the smallest RMSE when assessed against microscopy results (1.58 μm – Super CMV and 1.70 μm – EN31). This is comparable to the RMSE calculated for the GIXRD study in the literature [18] (1.7 μm). The penetration depth of x-rays, for 95% attenuation, in these two steel alloys is approximately 15.5 μm, as such both the white layer and the material beneath contribute to the resultant peak breadth. The peak breadth associated with a white layer surface in Super CMV is not identical to an EN31 white layer because the breadth also depends on the prior-processing history and therefore the near-surface plastic strain distribution prior to machining. This has important consequences for surface integrity inspection as it dictates that a calibration is required to define the threshold between a surface integrity pass and fail and to establish the mathematical relationship describing the dependence of peak breadth on feature thickness in a particular alloy or processing route. Such material and sizing calibration approaches are commonplace in non-destructive testing.

The vertical and horizontal error bars shown in Fig. 4 represent the standard deviation of the peak breadth and white layer microscopy thickness measurements respectively. The RMSE for the modelled sizing curve was slightly larger than the uncertainty from microscopy which was an average of 0.8 μm in the EN31 white layers and 0.4 μm in the Super CMV white layers. The results indicate that the single angle measurement approach could be utilised for rapid inspection in under 30 s and allows for truly non-destructive testing with diffractometer technology designed for inspection of real engineering components.

The micrographs of samples with very thin and thick white layers for each material, presented in Fig. 4, indicate that for EN31 surfaces with a white layer, there is a dark layer immediately beneath, whereas for Super CMV there is no dark layer. The diffraction patterns for three EN31 surfaces, Fig. 5 (a), show that for the surfaces with a white layer the intensity of the austenitic peaks is greater, indicating a higher retained austenite concentration compared to the surface without a white layer. By contrast, no evidence of austenite peaks in surfaces with or without a white layer is present for SMCV, as shown in Fig. 5 (b). This evidence indicates that PT white layers were formed in EN31 and SPD white layers were formed in Super CMV.

To investigate the use of different penetration depths to target resolution over different feature thickness ranges, the white layer samples were re-inspected using Cu and Ag x-rays such that the penetration depth was smaller or larger, respectively, than the maximum feature thickness, as shown in Fig. 6. RMSE values for sizing curves for each radiation are given in Table 4. The error in the sizing prediction is significantly reduced for the thin EN31 white layers when using Cu x-rays which have a small depth of penetration. By contrast, for the thicker Super CMV white layers, sizing accuracy is improved when using radiation that gives a larger penetration depth. Across all x-ray radiation sources, in general, the exponential model gave the greatest accuracies, closely followed by the linear model, with the constant model typically performing poorly.

The peak breadths measured during the inspection of the nickel superalloy samples are shown in Fig. 7. This sample set contained examples of plastic deformation between 5 and 60 μm and therefore encompassed features both smaller and thicker than the x-ray penetration depth (13.8 μm for 95% attenuation). The results show that XRD peak breadth is inherently sensitive to a significant difference between these surfaces for deformation levels up to the penetration depth. The measured peak breadth increases significantly with the swept grain thickness when it is smaller than 10 μm. It is readily observable from Fig. 7 that the CBN inserts from manufacturers four and three resulted in the lowest and highest peak breadths on average. These surfaces correspond to the smallest and largest deformation in these CBN trials, highlighting the potential of this NDT technique as a screening tool to quickly rank surfaces.

It can be seen from Fig. 7 that these swept grain surfaces have been fitted with models for exponential (Eq. (5)) and linear (Eq. (4)) decay of broadening through the feature thickness. The constant peak breadth model (Eq. (6)) was not used for swept grain as there is no evidence of strain remaining constant through this type of feature. The R-squared values for each sizing curve show that the linear decay model offers a better fit for the experimentally measured data across the whole range of samples but particularly for thin surface integrity features. This suggests the strain decays more linearly with depth rather than exponentially in these surfaces. Sizing estimation using the prediction curves for each model allows quantification of the plastic deformation thickness with an RMSE of 1.97 μm and 2.92 μm respectively when considering only the

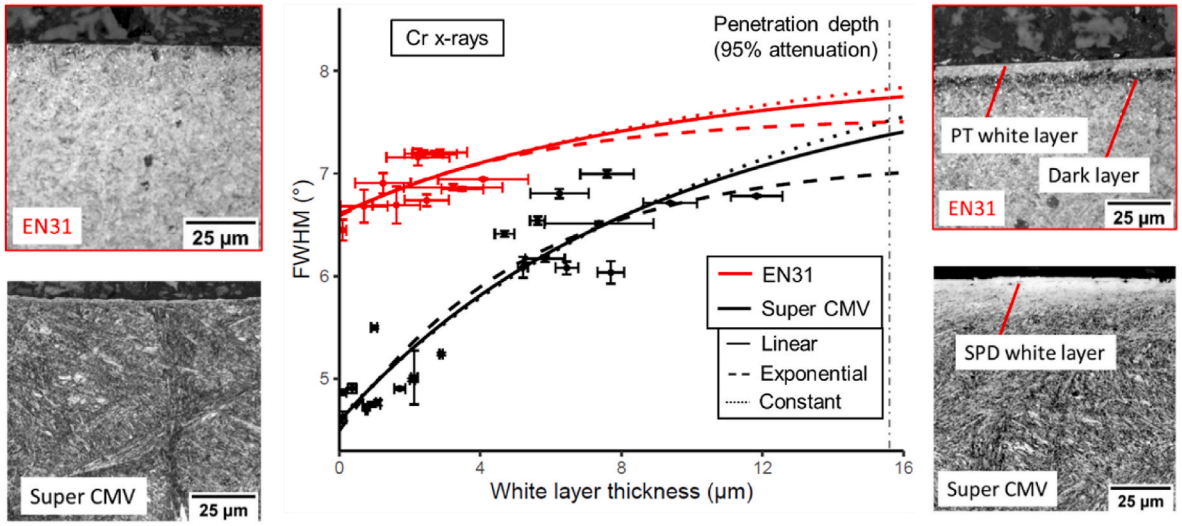

Fig. 4. Peak breadth plotted against white layer thickness for PT and SPD white layers in steel (penetration depth = 15.6 μm, Cr x-rays, Proto iXRD, (211) peak) with micrographs of surfaces with and without white layers in each alloy.

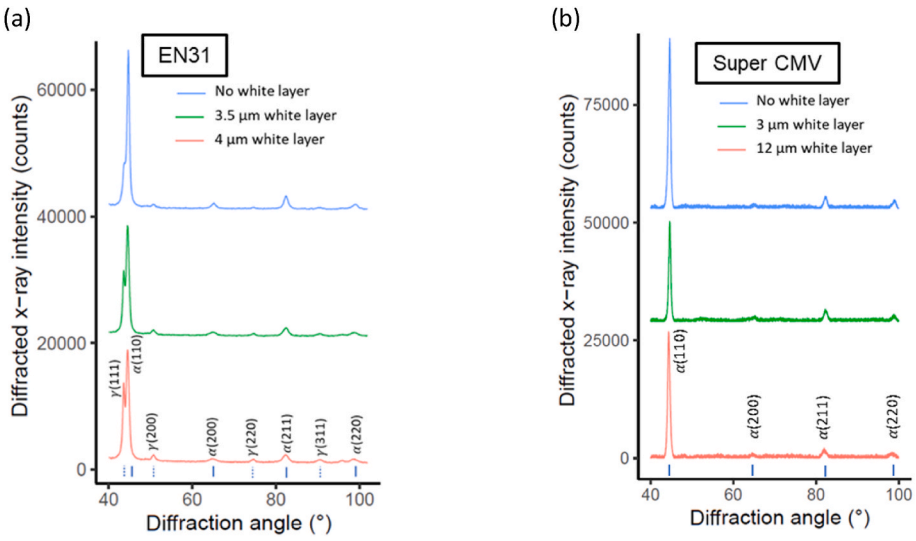

Fig. 5. Full XRD patterns for (a) EN31 and (b) Super CMV (Cu x-rays, X'Pert[3]).

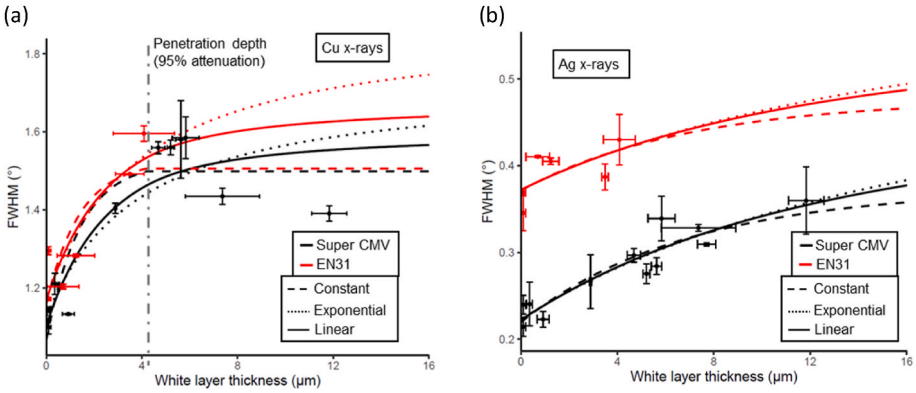

Fig. 6. The dependence of peak breadth on white layer thickness for (a) Cu x-rays (penetration depth = 4.2 µm, X'Pert[3]) and (b) Ag x-rays (penetration depth = 20.8 µm, Empyrean, (211) peak).

Table 4
RMSE values for prediction of layer thickness using different radiation and models.

	RMSE - linear (µm)			RMSE - exponential (µm)			RMSE - constant (µm)		
Material	Cu	Cr	Ag	Cu	Cr	Ag	Cu	Cr	Ag
Super CMV	3.11	1.62	1.48	2.94	1.58	1.42	3.49	2.30	2.27
EN31	0.44	1.70	1.64	0.44	1.69	1.64	0.41	1.82	1.66

features up to the penetration depth. For features larger than the penetration depth sizing is not possible due to the small changes in peak breadth for large changes in feature thickness. This RMSE for the linear model achieved with a single θ-2θ measurement is slightly larger than achieved using GI-XRD and measurements at different angles [18] so investigation of additional approaches is required to improve the sizing using single θ-2θ measurements.

Above the x-ray penetration depth, the peak breadth was larger than 6.4° for all surfaces inspected but does not change significantly with further increases in thickness, consequently a small change in measured peak breadth, on the order of the uncertainty of the XRD measurements, would lead to a significant change in predicted deformation. As such, peak breadth can therefore be used only as an indicator of severe plastic deformation in the near-surface, rather than for sizing thick features (>10 µm). The absence of a significant increase in peak breadth for samples from 20 µm up to 60 µm of deformed material suggests that, in these samples, a larger depth of deformation does not equate to significantly greater deformation in the x-ray inspection volume which would increase the strain broadening effect.

It is important to note that both models shown in Fig. 7 predict a low peak breadth for a sample with no deformation. However, near-surface deformation is an inherent result of the primary and tertiary shear zones during chip formation so a non-zero thickness of deformation would always be expected, meaning that obtaining such a sample was not possible in this study. It is not appropriate to use as-received material because, despite having no machining-induced deformation, it will have a near-surface strain pattern that is a function of the prior processing route and not indicative of a machine surface.

Whilst the linear decay model offers a reasonable approximation for the measured peak breadth across the whole thickness, it does not offer accurate sizing of deformation layers thicker than the penetration depth and the penetration depth is not optimised for the narrow range of thin

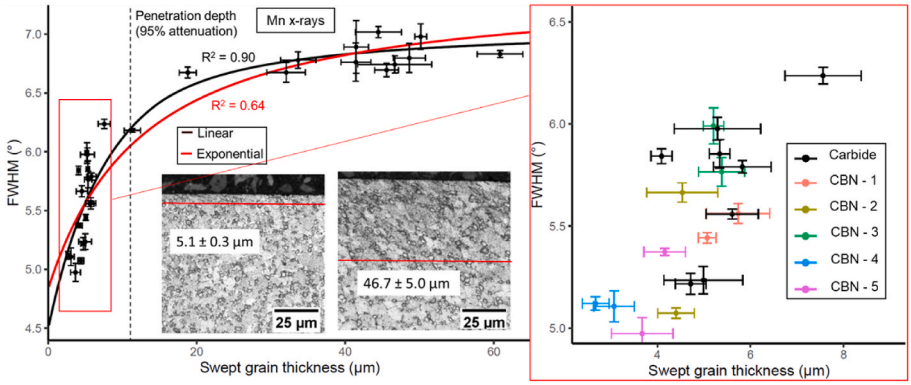

Fig. 7. Plots showing the dependence of peak breadth on the depth of plastic deformation in the machined surface for RR1000 samples for the full range of deformation depths and for features thinner than the x-ray penetration depth where the trials with CBN inserts are coloured by manufacturer (Mn x-rays, Proto iXRD, (311) peak). Examples of micrographs of a lightly and heavily deformed surface are provided with the swept grain thickness indicated.

features thicknesses present. To improve sizing at larger depths, alternate strategies for increasing the penetration depth must be investigated.

The peak breadth measured for the RR1000 sample set using Cu and Ag x-rays is shown in Fig. 8 (a) with the corresponding plot for Cu x-rays with different diffraction peaks shown in Fig. 8 (b). In both plots, the penetration depth is indicated and a linear decay model for sizing has been fitted. Corresponding RMSE values for the sizing curves are reported in Table 5. The absolute measured values of peak breadth are different between each radiation type and diffraction angle, due to different levels of instrument broadening for the diffractometers used as well as the reduced magnitude of strain and size broadening effect at lower diffraction angles. For deformation layers thicker than the penetration depth the peak breadth does not increase significantly for either radiation or diffraction peak. It is apparent that the larger penetration depth when using Ag x-rays is still not sufficient to allow accurate for large feature thicknesses and at most could extend the upper limit on sizing capability to 20 µm rather than 10 µm, however, further samples with deformation in this range would be required to confirm this. Ag x-rays are one of the highest energy options available for XRD and therefore there are no immediate alternatives for extending the penetration depth significantly further to allow sizing of deformation with a single measurement with lab-based equipment.

The use of Cu x-rays offers a significant improvement to sizing estimations compared to Mn and Ag x-rays due to its reduced penetration depth. Using a linear breadth decay model, the sizing curve has an RMSE of just 1.02 µm for thin features. Similarly, reducing the penetration depth by inspecting a diffraction peak with a lower diffraction angle can extract further sizing estimation improvements for thin features, with the (200) peak giving the lowest overall RMSE of 0.83 µm. This sizing estimation is only slightly larger than the average uncertainty in the microscopy measurements (0.5 µm) and as such, estimation to a higher accuracy using XRD will be limited by the achievable accuracy with the microscopy validation method. It is not possible to compare the variation in the peak breadth measurements from θ-2θ and GI-XRD as it is not clear whether repeats were undertaken in the GI-XRD study, however, it is apparent that appropriate selection of θ-2θ measurement parameters allows sizing estimation to comparable or improved accuracies relative to the GI-XRD methodology from Naskar and Paul [18] with rapid scan times.

Validation of the sizing curve approach to feature thickness was undertaken by training sizing curves based on a portion of XRD and microscopy measurements then predicting the size in the remaining surfaces based solely on the peak breath measurement. The RMSE for white layer and swept grain feature thickness prediction is summarised in Table 6 for different x-ray radiation, the error reported is the standard deviation of the RMSE values across all the training and validation partitions. The validation results confirm that sizing curves, based on x-ray diffraction theory applied to experimental data, can be used for accurate prediction of surface integrity feature thicknesses in different alloys, with different set-ups allowing inspection of different feature thickness ranges.

4. Discussion

Sizing using a single XRD measurement, in which the penetration

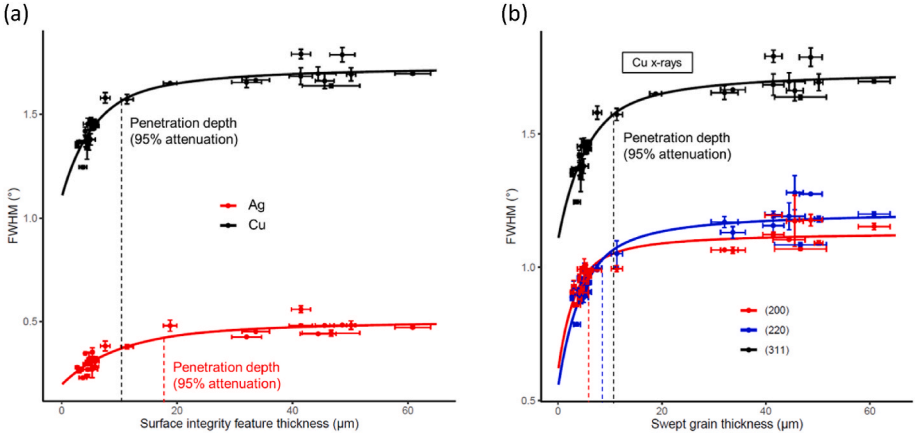

Fig. 8. A plots showing the peak breadth plotted against deformation depth in RR1000 samples for (a) Ag and Cu x-rays and (b) the (311), (220) and (200) peaks with Cu x-rays. The solid lines represent the modelled fit assuming a linear peak breadth decay for both radiation types.

Table 5
RMSE values for sizing curves when using different radiation and models.

	RMSE - linear (μm)					RMSE - exponential (μm)				
Material	Cu (311)	Cu (220)	Cu (200)	Mn (311)	Ag (311)	Cu (311)	Cu (220)	Cu (200)	Mn (311)	Ag (311)
RR1000	1.02	0.94	0.83	1.97	1.94	1.41	1.27	1.02	2.92	2.69

Table 6
RMSE values for prediction of layer thickness using sizing curves for different radiation.

	RMSE (μm)			
Feature sizing curve	Cu	Mn	Cr	Ag
Ni, Linear, (311)	1.09 ± 0.25	2.13 ± 0.49	N/A	1.87 ± 0.57
Ni, Linear, (200)	0.93 ± 0.15	N/A	N/A	N/A
Super CMV, Exponential, (211)	0.45 ± 0.34	N/A	1.54 ± 0.26	2.21 ± 1.04

depth is fixed for a particular combination of material, x-ray radiation and diffraction peak, is possible due to the exponential decay of x-ray intensity with depth. The measured peak breadth is a function of the peak breadth of all the material within the x-ray interaction volume and due to the decay of x-rays with depth, the near-surface material has a greater influence on the measured peak breadth than the material at larger depths. For thicker features, the feature occupies a greater proportion of the interaction volume and so the measured peak breadth is greater. Detection and sizing of SPD and PT white layers is facilitated by the sensitivity of XRD peak breadth to the small grain structure and high levels of plastic strain present within white layers. By contrast, the sensitivity to swept grain is due only to the presence of plastic strain within material near the surface up to the XRD penetration depth.

It has been shown that assuming a linear or exponential decay of strain broadening effects across the white layer or swept grain thickness allows quantification of size to within 0.5–2 μm with a single peak breadth measurement, for layers thinner than the penetration depth. Further improvements in accuracy could potentially be made by allowing the modelled peak breadth at the machined surface to increase with the feature thickness and by considering resultant peak breadth across a feature in terms of the superposition of multiple pseudo-Voigt peaks, rather than simply the weighted sum of the peak breadths. Sizing of thicker features can only be achieved by using different radiation, peaks or incidence angles to increase the penetration depth. However, XRD tubes with higher energies than Ag x-rays are not typically available for commercial systems, which places an upper limit on the maximum feature thickness that could be sized for a particular material. Whilst the angle of incidence can be used to change the penetration depth, as has been shown when sizing grinding deformation using GI-XRD [18], the penetration depth is maximum in θ-2θ geometry so cannot be increased further. Likewise, a different diffraction peak can used to change the penetration depth, but useful inspection is limited to diffraction peaks that can be resolved above the background intensity and in this study this measurement strategy did not allow sizing of large features.

Whilst changing the radiation proved effective for improving sizing accuracies across different length scales, the use of different diffraction peaks was less effective. Using different diffraction peaks introduces errors associated with peak broadening anisotropy. It has already been shown that the peak breadth and the ability to distinguish between damaged and undamaged surfaces varies with the diffraction peak [17]. Whilst some of this difference can be attributed to penetration depth differences, peak breadth is also affected by factors such as the anisotropy of elastic modulus [27] as well as the activation of different slip systems during deformation, which means different types of dislocation can be responsible for lattice strain in different grains [28]. As such, changing the radiation is a more desirable method for sizing using different penetration depths as the same crystallographic plane can be examined, eliminating anisotropy effects.

The key benefits and limitations of XRD, GI-XRD and microscopy are outlined in Table 7. Whilst XRD based techniques are non-destructive, the diffractometer optics required for high quality GI-XRD measurements can necessitate destructive sectioning to be able to fit the machined surface in the diffractometer, in the path of the x-ray beam. Whilst no sample preparation is required for XRD, microscopy inspection involves time-consuming preparation steps significantly increasing the overall inspection time. Conventional XRD offers significant measurement time improvements over the GI-XRD method due to the ability to capture useful information from only a single scan rather than requiring multiple scans at different diffraction angles to determine size. Additionally, GI-XRD requires a higher resolution diffractometer with beam optics to obtain high-quality measurements in which the broadening effects of the small angle of incidence and large illumination area are reduced.

Microscopy is inherently a post-process, offline inspection method but conventional XRD offers the potential for on-machine, in process, inspection with the development of appropriate equipment. This is desirable in modern manufacturing as it could eventually facilitate inspection being undertaken as part of a lights-out production method. The results from inspection could be readily incorporated into the digital twin for a particular component allowing informed decisions to be made on the quality of the part.

XRD based methods produce quantitative results with no

Table 7
A summary of the benefits and limitations of microscopy against XRD and GI-XRD.

Technique	Microscopy	XRD FWHM	GI-XRD FWHM
Non-destructive	No	Yes	Depends on surface
Prep time	Hours - Days	None	Potential sectioning time
Measurement time	Minutes	<1 min	Minutes-Hours
Equipment	Metallographic preparation, Microscopy, Fume cupboard	X-ray diffractometer, no beam optics needed	X-ray diffractometer with beam optics
In-process inspection	No	Possible	No, due to need for multiple angles
Geometry limitations	None	Curvature (<5 mm radius of curvature), surface access (internal diameters, macro surface waviness)	Curvature, surface waviness and roughness, internal diameters. Component must fit within diffractometer
Health & Safety	Chemical etching	Ionising radiation	Ionising radiation
Analysis type	Quantitative, requires operator interpretation	Quantitative, objective	Quantitative, objective
Resolution	1 μm, no calibration required	1–2 μm, with material calibration	1–2 μm, with material calibration
Surface coverage	Line	Area	Area

requirement for inspector interpretation, this is a significant advantage over microscopy which, despite having high resolution, require inspector interpretation to determine the extent of a feature, which can lead to significant sources of variation. Additionally, microscopy captures only the surface integrity across a plane at the point of sectioning on the machined surface, whereas XRD covers an area and this offers a quicker route to generating a spatial assessment of aspects of surface integrity and increases the chance of finding an intermittent surface integrity feature.

This study has shown that XRD peak breadth assessment of surface integrity has the potential to be used for rapid surface integrity validation of critical components where the formation of white layers or severe plastic deformation in the processed surface is unacceptable. The NDT method could also find use a screening tool during process optimisation. The technique allows machined surfaces to be ranked according to their level of surface damage, thereby allowing a down-selection of the conditions used to generate the best surfaces for further testing. By removing the need for destructive sectioning, optimisation trials can then be undertaken immediately, enabling faster process development, relative to sending all samples for destructive microscopy when the microstructural surface integrity is an important metric.

5. Conclusions

This research was undertaken to investigate the application of x-ray diffraction for truly non-destructive, rapid inspection of common aero-engine alloys to size machining-induced white layers and plastic deformation. For features thinner than the x-ray penetration depth, sizing can be achieved to within 0.5–2 μm of the thickness measured with optical microscopy with inspection undertaken in a matter of seconds, rather than the hours or days required for microscopy. The key findings of the work can be summarised as follows:

- SPD and PT white layers can be sized due to the sensitivity of XRD peak breadth to their intrinsic small grain size and high strain. By contrast, sizing of swept grain is only achievable due to strain effects as the grain structure is too large to result in significant broadening.
- Sizing of white layers and swept grain can be achieved to within 0.5–2 μm of the value measured during microscopy for features up to the x-ray penetration depth. This is achieved with a sizing curve generated from experimental data which can be applied to predict future measurements. The curve assumes exponential or linear decay of peak broadening with depth beneath the machined surface.
- Surface integrity feature sizing can be achieved with portable diffraction equipment allowing truly non-destructive measurements on a wide range of component size and shapes with inspection times of under 1 min.
- The uncertainty in the XRD peak breadth sizing estimations is comparable to that recorded during optical microscopy assessment, due to variation in surface integrity between different locations in the region in under assessment and the subjectivity of operator interpretation.
- Measurements of peak breadth over a large range of feature thicknesses allow a depth-dependence of strain in the surface to be estimated. In this study, for example, it was measured that a linear strain decay with depth in the machined surfaces was a better approximation than exponential decay for samples with swept grain.
- Accurate sizing of features thicker than the penetration depth is not possible in the samples investigated. However, the penetration depth can be tuned by altering the x-ray radiation, diffraction peak to give improved sizing accuracy for different feature thickness ranges. For very thin features, a small x-ray penetration depth improves accuracy.

Funding

This work was supported by HVM Catapult funding provided by Innovate UK. A number of the machined surfaces used in this study were generated alongside Rolls-Royce PLC and Seco Tools and the authors wish to extend thanks to them.

Declaration of competing interest

The authors declare that they have no known competing financial interests or personal relationships that could have appeared to influence the work reported in this paper.

References

[1] Guo YB, Warren AW, Hashimoto F. The basic relationships between residual stress, white layer, and fatigue life of hard turned and ground surfaces in rolling contact. CIRP J Manuf Sci Technol 2010;2(2):129–34.
[2] Herbert C, et al. Influence of surface anomalies following hole making operations on the fatigue performance for a nickel-based superalloy. J Manuf Sci Eng 2014; 136(5):51016. 1-9.
[3] Griffiths BJ. Mechanisms of white layer generation with reference to machining and deformation processes. J Tribol 1987;109(3):525–30.
[4] Guo YB, Ammula SC. Real-time acoustic emission monitoring for surface damage in hard machining. Int J Mach Tool Manufact 2005;45(14):1622–7.
[5] Barry J, Byrne G. TEM study on the surface white layer in two turned hardened steels. Mater Sci Eng, A 2002;325(1–2):356–64.
[6] Wusatowska-Sarnek AM, et al. Microstructural characterization of the white etching layer in nickel-based superalloy. Metall Mater Trans 2011;42(12):3813–25.
[7] Kwong J, Axinte DA, Withers PJ. The sensitivity of Ni-based superalloy to hole making operations: influence of process parameters on subsurface damage and residual stress. J Mater Process Technol 2009;209(8):3968–77.
[8] Hosseini SB, et al. Cutting temperatures during hard turning—measurements and effects on white layer formation in AISI 52100. J Mater Process Technol 2014;214 (6):1293–300.
[9] Hosseini SB, et al. Formation mechanisms of white layers induced by hard turning of AISI 52100 steel. Acta Mater 2015;89:258–67.
[10] Edkins KD, Rensburg NJv, Laubscher RF. Evaluating the subsurface microstructure of machined Ti-6Al-4V. Procedia CIRP 2014;13:270–5.
[11] Klocke F, et al. Influence of temperature on surface integrity for typical machining processes in aero engine manufacture. Procedia Eng 2011;19:203–8.
[12] Xu D, et al. A novel method to continuously map the surface integrity and cutting mechanism transition in various cutting conditions. Int J Mach Tool Manufact 2020;151:103529.
[13] Crawforth P, et al. Subsurface deformation during precision turning of a near-alpha titanium alloy. Scripta Mater 2012;67(10):842–5.
[14] Sela A, et al. Surface drag analysis after Ti-6Al-4V orthogonal cutting using grid distortion. Procedia CIRP 2020;87:372–7.
[15] Zhou JM, et al. Effects of tool wear on subsurface deformation of nickel-based superalloy. Procedia Eng 2011;19:407–13.
[16] Brown M, et al. On deformation characterisation of machined surfaces and machining-induced white layers in a milled titanium alloy. J Mater Process Technol 2022;299:117378.
[17] Brown M, et al. Non-destructive detection of machining-induced white layers through grain size and crystallographic texture-sensitive methods. Mater Des 2021; 200:109472.
[18] Naskar A, Paul S. Non-destructive measurement of grinding-induced deformation-depth using grazing incidence X-ray diffraction technique. NDT & E International; 2021, 102592.
[19] Brown M, et al. Quantitative characterization of machining-induced white layers in Ti–6Al–4V. Mater Sci Eng, A 2019;764:138220.
[20] Cullity BD. Elements of X-ray diffraction. *Addison*. Wesley Mass; 1978.
[21] Empyrean. [cited 2022 January]; Available from: malvernpanalytical.com/en/products/product-range/empyrean-range/empyrean.
[22] Bragg WH, Bragg WL. The reflection of X-rays by crystals. In: Proceedings of the royal society of London. Series A, containing papers of a mathematical and physical character. 88; 1913. p. 428–38. 605.
[23] Guo Y, et al. Controlling deformation and microstructure on machined surfaces. Acta Mater 2011;59(11):4538–47.
[24] Brown M, et al. Non-destructive detection of machining-induced white layers in ferromagnetic alloys. Procedia CIRP 2020;87:420–5.
[25] Ramesh A, et al. Analysis of white layers formed in hard turning of AISI 52100 steel. Mater Sci Eng, A 2005;390(1–2):88–97.
[26] Poulachon G, et al. An experimental investigation of work material microstructure effects on white layer formation in PCBN hard turning. Int J Mach Tool Manufact 2005;45(2):211–8.
[27] Stephens PW. Phenomenological model of anisotropic peak broadening in powder diffraction. J Appl Crystallogr 1999;32(2):281–9.
[28] Wilkens M. X-ray line broadening and mean square strains of straight dislocations in elastically anisotropic crystals of cubic symmetry. physica status solidi (a) 1987; 104(1):K1–6.